



HAL
open science

Aiming strategy optimization for uniform solar flux distribution in the receiver of a linear Fresnel reflector using genetic algorithm

Yu Qiu, Ya-Ling He, Han-Hui Zhu, Kai Zhang

► To cite this version:

Yu Qiu, Ya-Ling He, Han-Hui Zhu, Kai Zhang. Aiming strategy optimization for uniform solar flux distribution in the receiver of a linear Fresnel reflector using genetic algorithm. 2016. hal-01413599v1

HAL Id: hal-01413599

<https://hal.science/hal-01413599v1>

Preprint submitted on 10 Dec 2016 (v1), last revised 17 Nov 2017 (v3)

HAL is a multi-disciplinary open access archive for the deposit and dissemination of scientific research documents, whether they are published or not. The documents may come from teaching and research institutions in France or abroad, or from public or private research centers.

L'archive ouverte pluridisciplinaire **HAL**, est destinée au dépôt et à la diffusion de documents scientifiques de niveau recherche, publiés ou non, émanant des établissements d'enseignement et de recherche français ou étrangers, des laboratoires publics ou privés.

Aiming strategy optimization for uniform solar flux distribution in the receiver of a linear Fresnel reflector using genetic algorithm

Yu Qiu, Ya-Ling He*, Han-Hui Zhu, Kai Zhang

(Key Laboratory of Thermo-Fluid Science and Engineering of Ministry of Education, School of Energy and Power Engineering, Xi'an Jiaotong University, Xi'an, Shaanxi, 710049, China)

Abstract: Energy maldistribution and local high flux may lead to negative effects, including the fluctuating operation and failure of the receiver, in linear Fresnel reflectors. For reducing these effects, an aiming strategy optimization approach for homogenizing the flux distributions in the receivers is presented by combining Monte Carlo ray tracing and Genetic Algorithm (GA). Based on the model, firstly, the flux distributions in both the Multi-Tube Cavity Receiver (MTCR) and the Single-Tube Receiver with a Secondary Collector (STRSC) are optimized at the typical condition. The optimization results indicate that the GA approach helps to reduce the energy maldistribution among the tubes in MTCR and homogenize the fluxes in both MTCR and STRSC significantly, where the energy maldistribution index of 3.1% in MTCR and the flux non-uniformity index of 13.5% in STRSC are achieved, and the corresponding peak fluxes are reduced by 59.3% and 46.4% compared to those of traditional one-line aiming strategy, respectively. Furthermore, parameter study indicates that proper values for the width of the aiming plane and the number of the aiming lines, which influence the flux distribution importantly, should be designed for reaching a compromise between the flux distribution and efficiency. Finally, application of the approach under a real-time condition indicates that satisfactory optimization results can be obtained in the whole range of the incident angle for the sun rays. It is concluded that the present GA approach is effective and suitable for optimizing the solar flux distributions in the receivers of LFRs.

Keywords: Linear Fresnel solar reflector; Aiming strategy optimization; Energy maldistribution; Non-uniform solar flux; Monte Carlo ray tracing; Genetic algorithm

1. Introduction

The combustion of fossil fuels has resulted in not only the tight global energy supply but also serious global environment issues like air pollution and global warming[1-6]. For solving these problems, renewable energy technologies, including Concentrating Solar Power (CSP)[7], photovoltaic[8], wind power[9], hydropower[10], geothermal power[11], ocean power[12], biomass

energy technology[13], hydrogen energy and fuel cell technology[14, 15], etc., are considered to be highly competitive candidates[16]. Among these candidates, the CSP technology which mainly includes Linear Fresnel Reflector (LFR)[17], parabolic trough collector[18-22], solar power tower[23-27], and parabolic dish collector[28-30] is considered as a promising option[31-33].

LFR technology is a medium-low temperature solar power technology which has attracted increasing attention in recent years. In a LFR, solar radiation is concentrated onto a fixed receiver by several linear mirrors, where the receiver is usually a Single-Tube Receiver with a Secondary Collector (STRSC)[34] or a Multi-Tube Cavity Receiver (MTCR)[35]. The optical performance of a LFR which determines the input power of the system is important for system design, performance optimization and safe operation. Hence, many studies have focused on this topic in recent times.

On the one hand, some studies on LFRs using STRSCs have been carried out. Häberle et al.[36] evaluated the optical performance of the first LFR plant Solarmundo which uses a secondary Compound Parabolic Collector (CPC). It is found that the optical efficiency of 61% is achieved at normal incidence, and the circumferential flux on the absorber tube is non-uniform. Qiu et al.[37] also studied the optical characteristics of a LFR using a STRSC with a CPC by a self-developed Monte Carol ray tracing (MCRT) model. It is found that the circumferential flux can be homogenized by the CPC with 34% of the total power on the top half of the tube. Similar non-uniform fluxes have also been obtained by Balaji et al.[38] and Craig et al.[39]. Moreover, Grena and Tarquini[40] designed a new double-wing secondary collector. The simulated result shows that the circumferential flux on tube is also non-uniform, and about 37% of the total power is shone on the top half.

On the other hand, some studies on LFRs using MTCRs have also been conducted. Mills and Morrison[41] proposed a novel design called compact linear Fresnel reflector which offers two alternative receivers to each mirror. Optical study depicts that a non-uniform flux on the receiver is observed. Qiu et al.[42] and Moghimi et al [43] computed the fluxes on MTCRs in LFRs using MCRT method and finite volume method, respectively. Both studies found that the rays almost just shine on the lower half of the tubes, which results in the non-uniform flux on each tube. It was also found that the energy maldistribution among the tubes is significant. Abbas et al.[44-46] and Bellos et al.[47] investigated the concentration features on flat receivers by MCRT method and Solidworks, respectively, where the flat receivers can be seen as the apertures of MTCR and STRSC. It was

found that the flux on the flat receiver is significantly non-uniform with a hot region at the center.

To sum up, it can be seen that non-uniform circumferential flux appears on each tube in both the STRSC and the MTCR. As a result, this flux will result in the non-uniform temperature on every tube[37, 48], and it may lead to two further negative effects. The first one is that the local high temperature may accelerate the degradation of coating on tube and the decomposition of heat transfer fluid[49, 50]. The second one is that the large thermal stress caused by temperature gradient may lead to undesirable distortions and damage of the receiver[49], especially when the evacuated tube is used. It is also found that the energy maldistribution among tubes occurs in the MTCR, which may results in the unstable operation due to the uneven heating of the fluid among the tubes.

For weakening these negative effects, it is necessary to improve the circumferential flux uniformity on a tube and reduce the energy maldistribution among tubes. Review of literatures indicates that few studies have focus on this topic, and only Eck et al.[50] had indicated that solar flux on the absorber tube can be reduced by defocusing mirror-to-mirror.

To provide better studies for solving these problems, this work focuses on developing an optimization approach using Monte Carol ray tracing (MCRT) and Genetic algorithm (GA) for homogenizing the circumferential flux and reducing the energy maldistribution in receivers of LFRs. After validation, the approach is applied in LFRs with both STRSC and MTCR, and effects of critical factors are also further investigated.

2. Physical model and aiming strategies

A LFR primary mirror field with 25 cylindrical mirrors is taken as the concentrator[37, 42]. A Multi-Tube Cavity Receiver (MTCR)[42] and a Single-Tube Receiver with a Secondary Collector (STRSC)[37] are considered as the receiver module, respectively. The configuration of the LFR is illustrated in Fig. 1 and Fig. 2, and the LFR is assumed to be located at the typical latitude of $\varphi=N23.5^\circ$. The geometric and optical parameters are shown in Table 1. The mirror field is symmetrical about its middle line, and two mirrors at symmetric positions have the same the dimensions. The central mirror and the eastern mirrors are numbered M1 to M13 from the west to the east as shown in Fig. 1, and the western mirrors are numbered M14 to M25 from the east to the west. The mirrors with non-constant curvatures were used for concentrating as much power as possible, and the curvature radiuses R_m for the eastern 13 mirrors are given in Eq.(1). The MTCR

which includes eight absorber tubes is covered by a glass plate at the bottom and by aluminum walls and asbestos on the top. The STRSC includes a Compound Parabolic Collector (CPC) and an evacuated tube. The equations of the CPC profile in Fig. 2(b) are expressed in Eqs.(2) and (3)[37].

$$R_m(i) = \begin{cases} 16.1 + (i-1)[0.10 + 0.10(i-2)], & 1 \leq i \leq 7 \\ 14.3 + (i-1)[0.65 + 0.05(i-2)], & 8 \leq i \leq 13 \end{cases} \quad (1)$$

$$\begin{cases} y_r = \rho_o \cos \theta_o - r_1 \sin \theta_o \\ z_r = \rho_o \sin \theta_o + r_1 \cos \theta_o \end{cases} \quad (2)$$

$$\begin{aligned} AB: \rho_o &= r_1(\theta_o + \beta), \arccos\left(\frac{r_1}{r_2}\right) \leq \theta_o \leq \frac{\pi}{2} + \theta_a \\ BC: \rho_o &= \frac{r_1[\pi/2 + \theta_o + \theta_a + 2\beta - \cos(\theta_o - \theta_a)]}{1 + \sin(\theta_o - \theta_a)}, \\ &\pi/2 + \theta_a < \theta_o \leq \theta_{o\max} \\ \beta &= \sqrt{(r_2/r_1)^2 - 1} - \arccos(r_1/r_2) \end{aligned} \quad (3)$$

where i is the ordinal number of the eastern 13 mirrors.

Several Cartesian coordinate systems, including the incident-normal system ($X_i Y_i Z_i$), the ground system ($X_g Y_g Z_g$), the mirror system ($X_m Y_m Z_m$) and the receiver system ($X_r Y_r Z_r$), are established in Fig. 1 and Fig. 2 for describing the model. In $X_i Y_i Z_i$, the intersection of the incident ray and the mirror is the origin. Z_i points towards the sun, and X_i is horizontal and perpendicular to Z_i . Y_i is normal to $X_i Z_i$ plane and points upwards. Other systems and the relations among all systems are clearly illustrated in Fig. 1 and Fig. 2.

The aiming line (X_g, y_{aim}, z_{aim}) in $X_g Y_g Z_g$ for a mirror is the line on the receiver hit by the rays reflected on the center line of the mirror. There are two basic aiming strategies for LFRs as illustrated in Fig. 2. One is the one-line aiming strategy named after S1, where all mirrors aim at the center line of the receiver, i.e., $y_{aim}=0$ and $z_{aim}=H_t$ in current LFR. The other is the multi-line aiming strategy (S2), where 25 lines are uniformly distributed across the plane of $z_{aim}=H_t$. The aim lines for the mirrors at symmetrical locations are symmetrical about the $X_g Z_g$ plane, and y_{aim} of the eastern 13 mirrors are given in Eq.(4)[42].

In current work, a new aiming strategy (S3) is presented as shown in Fig. 2. In S3, n_{aim} aiming lines are uniformly distributed on the plane of $z_{aim}=H_t$ and numbered A1 to $A_{n_{aim}}$ from the west to the east. Each mirror would choose a line randomly from the n_{aim} lines, and the aiming strategy for

all the mirrors would be optimized by employing genetic algorithm for distributing the solar power on the tubes uniformly.

$$y_{\text{aim}} = \begin{cases} 0 & , i=1 \\ -0.5W_{\text{aim}} + (i-2)\frac{W_{\text{aim}}}{24} & , 2 \leq i \leq 13 \end{cases} \quad (4)$$

where W_{aim} is the width of the aiming plane; i is the ordinal number of the aiming lines.

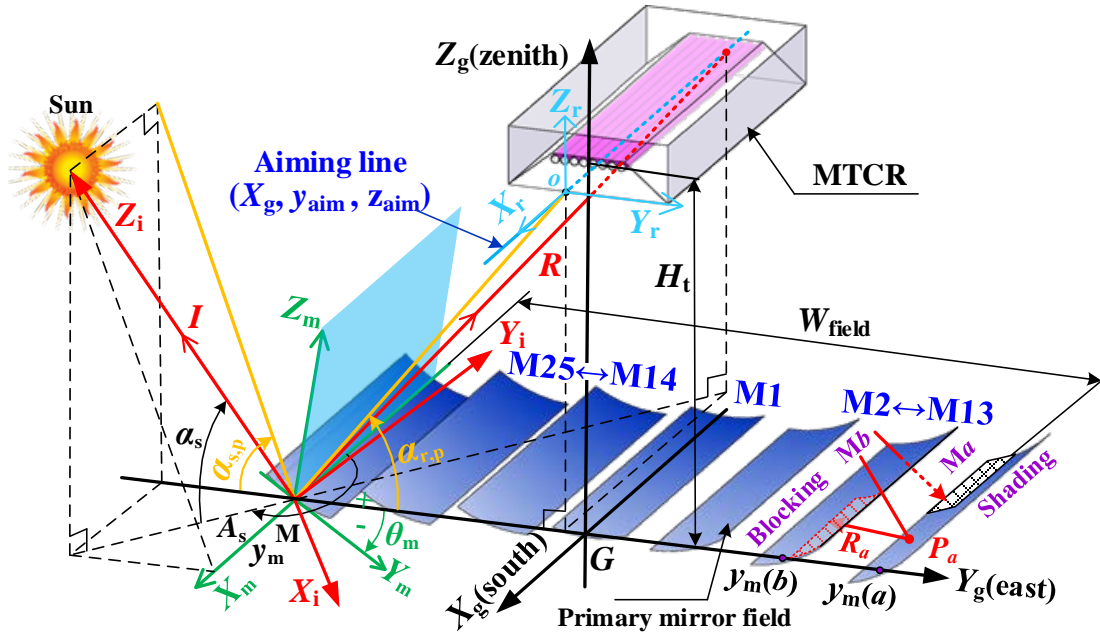
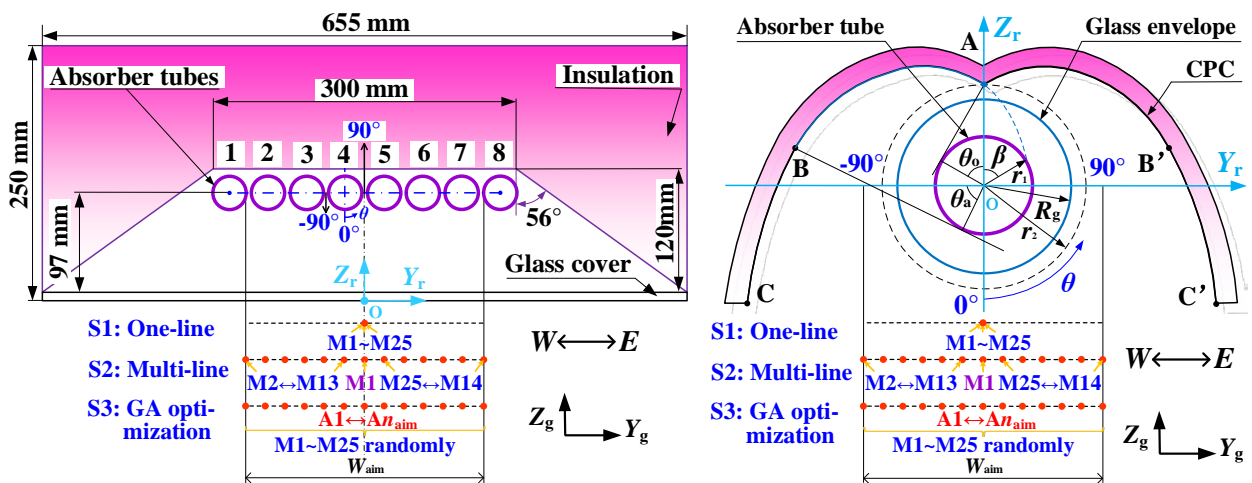


Fig. 1. Sketch of a LFR showing the solar ray transfer.



(a) Multi-Tube Cavity Receiver (MTCR). (b) Single-Tube Receiver with a Secondary Collector (STRSC).

Fig. 2. Sketches of two receivers showing three aiming strategies.

Table 1 Geometric and optical parameters of the LFR [35, 36, 51, 52].

Parameters	Value	Parameters	Value
Primary mirror number n_m	25	Diffuse reflectance of MTCR's wall $\rho_{w,d}$	0.77
Width of the field W_{field}	20.4 m	Coating absorptivity in MTCR α_t	0.93
Width of the mirror W_m	0.6 m	Coating diffuse reflectance in MTCR $\rho_{t,d}$	0.04
Length of collector L_m	100 m	Aperture width of CPC	295 mm
Distance between two mirrors	0.85 m	Thickness of CPC	5 mm
Specular reflectance of mirror ρ_m	0.92	Half acceptance angle of CPC θ_a	56°
slope error of mirror and CPC σ_{se}	1.0 mrad	θ_{omax}	3.37 rad
Height of the tube in LFR H_t	8.0 m	r_2	62.5 mm
Cavity's bottom width of MTCR	655 mm	Tube's outer radius in STRSC r_1	35 mm
Cavity's top width o of MTCR	300 mm	Envelope's outer radius R_g	57.5 mm
Half acceptance angle of MTCR	56°	Thickness of envelope	3 mm
Depth of MTCR	120 mm	Specular reflectance of CPC	0.95
Tube number of MTCR n_t	8	Absorptivity of CPC	0.05
Tube outer diameter in MTCR	36 mm	Glass transmittance/absorptivity τ_g, α_g	0.96/0.02
Gap between two tubes in MTCR	3 mm	Glass specular reflectance ρ_g	0.02
Glass cover thickness in MTCR	3 mm	Glass refraction index n_g	1.47
Absorptivity of MTCR's wall α_w	0.15	Coating absorptivity in STRSC α_t	0.96
Specular reflectance of MTCR's wall $\rho_{w,s}$	0.08	Coating diffuse reflectance in STRSC $\rho_{t,d}$	0.04

3. Mathematical model

As mentioned before, the maldistribution of the solar power among the tubes and the local high flux could result in a series of problems. To reduce the maldistribution and lower the high flux, the aiming strategy was optimized by combining a Monte Carol ray tracing (MCRT) model and Genetic Algorithm (GA). The flowchart of the optimization is shown in Fig. 3. In the optimization, the MCRT model is used to compute the power absorbed on each tube and predict the flux on the tube. GA is used to evaluate and optimize the power distribution in the receiver. For the STRSC, a non-uniformity index of the circumferential flux (f_{ST}), which is defined as the relative standard deviation of the values of the flux in the circumferential elements on the absorber tube, is defined as the fitness/objective function in Eq.(5). For the MTCR, an energy maldistribution index (f_{MT}) which is defined as the relative standard deviation of the values of the power absorbed on the tubes is defined as the fitness function in Eq.(6). The detailed model is explained in the following sections.

$$f_{ST} = \frac{\sqrt{\sum_{i=1}^{n_e} [q_1(i) - \bar{q}_1]^2 / (n_e - 1)}}{\bar{q}_1} \times 100\%, \bar{q}_1 = \frac{\sum_{i=1}^{n_e} q_1(i)}{n_e} \quad (5)$$

$$f_{MT} = \frac{\sqrt{\sum_{i=1}^{n_t} [E_t(i) - \bar{E}_t]^2 / (n_t - 1)}}{\bar{E}_t} \times 100\%, \bar{E}_t = \frac{\sum_{i=1}^{n_t} E_t(i)}{n_t} \quad (6)$$

where n_e is the number of the circumferential elements on the tube in STRSC; n_t is the number of the tubes; $q_1(i)$ is local flux in i th element; $E_t(i)$ is the power absorbed by i th tube.

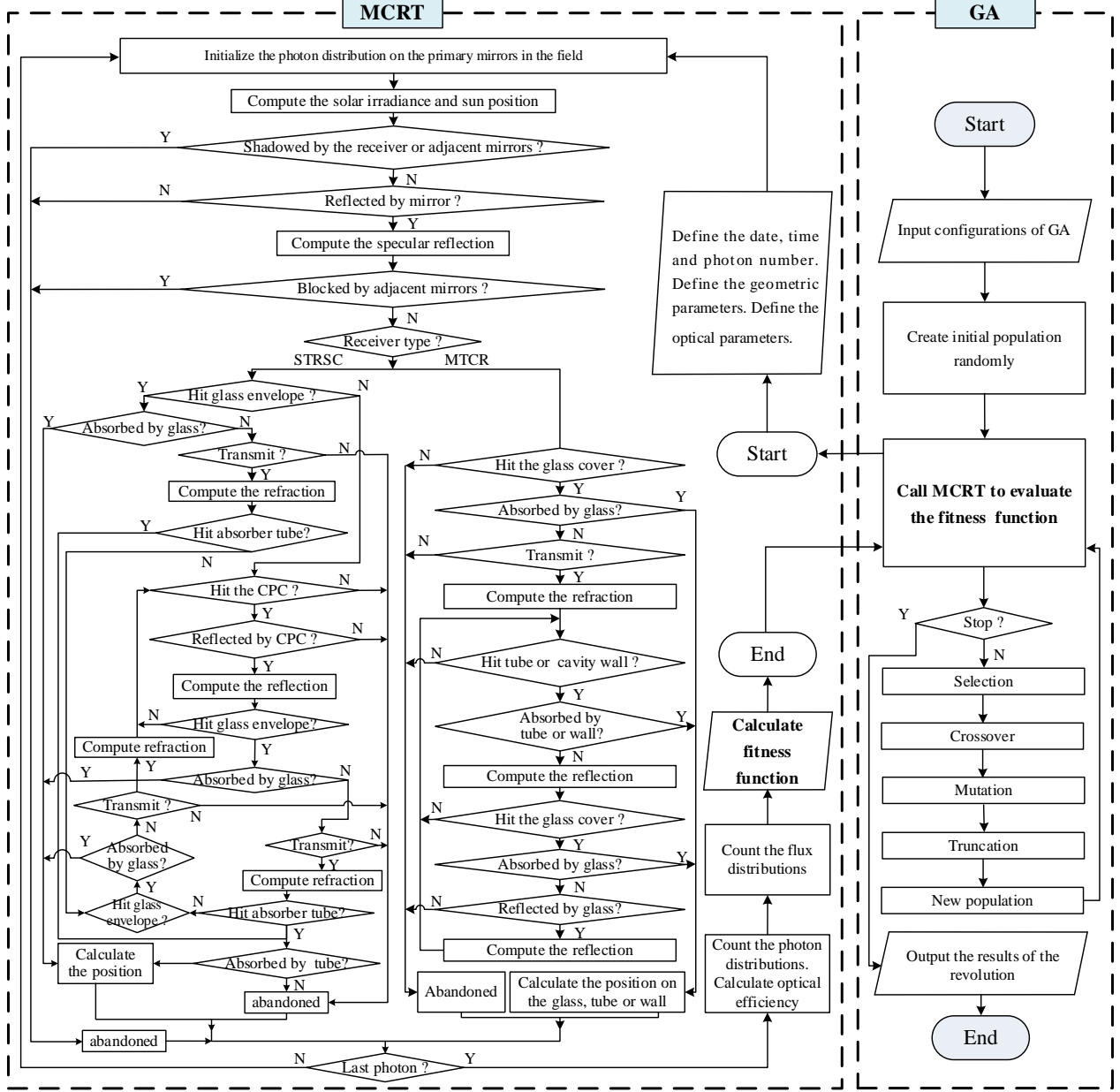


Fig. 3. Flowchart for the code of the GA aiming strategy optimization approach.

3.1 Optical model based on Monte Carol ray tracing

The solar ray transfer from the sun to the receiver can be divided in two processes which are the process in the primary mirror field and the process in the receiver. These processes are simulated by a three-dimensional optical model developed based on Monte Carol ray tracing method (MCRT). The code was programmed in FORTRAN, and the flowchart is illustrated on the left side of Fig. 3.

The model is detailed as follows.

3.1.1 Tracking equations and solar model

The tracking angle for a mirror (θ_m) is defined as the angle between the positive directions of Y_m and Y_g . In the northern hemisphere, the tracking angle θ_m for a western mirror is given in Eq.(7). θ_m at other conditions can be obtained in the similar way[37].

$$\theta_m = 0.5 \cdot (\alpha_{r,p} - \alpha_{s,p}) \quad (7)$$

$$\alpha_{s,p} = \tan^{-1} \left(\frac{\tan \alpha_s}{\sin |A_s - \pi|} \right), \alpha_{r,p} = \tan^{-1} \left| \frac{z_{aim}}{y_{aim} - y_m} \right| \quad (8)$$

where y_m is the y value of the mirror center line in $X_g Y_g Z_g$; α_s and A_s are the solar altitude and azimuth, which can be obtained when the local latitude φ , real solar time t_s and the ordinal of a day in a year are provided[42]; $\alpha_{s,p}$ is called the solar altitude's projection which is the angle between the projection of the unit incident vector of a ray (\mathbf{I}) on $Y_g Z_g$ plane and Y_g ; $\alpha_{r,p}$ is the angle between the projection of the reflected vector (\mathbf{R}) on $Y_g Z_g$ plane and Y_g .

The solar rays are initialized randomly and uniformly on the mirrors[37]. The sun shape error is considered as a pillbox with an angular radius of $\delta_{sr}=4.65$ mrad. So, the unit vector (\mathbf{I}) of an incident ray can be expressed as Eq.(9) in $X_i Y_i Z_i$ [42]. The Direct Normal Irradiance (DNI) of the sun in a year is calculated by a clear sky radiation model[53], and the power of each ray (e_p) is calculated by Eq.(10).

$$\mathbf{I} = \left[\delta_s \cdot \cos \theta_s \quad \delta_s \cdot \sin \theta_s \quad \sqrt{1 - \delta_s^2} \right]^T \quad (9)$$

$$\delta_s = \sin^{-1} \left(\sqrt{\xi_1 \cdot \sin^2 \delta_{sr}} \right), \theta_s = 2\pi \cdot \xi_2$$

$$e_p = DNI \cdot L_m W_m \sum_{i=1}^{n_m} \eta_{\cos}(i) / N_p \quad (10)$$

where $\eta_{\cos}(i)$ is the cosine efficiency of the i th mirror; N_p is the number of the total rays; each ξ_i is a uniform random number between 0 and 1 in current text, i.e. $\xi_i \sim U[0,1]$.

3.1.2 Simulation of the solar ray transfer in the mirror field

When a ray hits the mirror in the field, the specular reflection will be calculated. Firstly, the optical process is randomly decided by Eq.(11) using a random number (ξ_3). Then, if the ray is reflected, Fresnel's law of specular reflection will be used to calculate the reflected vector, where the

slope error of the mirror surface is assumed to follow a Gaussian distribution and would introduce a deviation in the reflection direction of the ray[37]. The reflection on the CPC in STRSC can be computed in the similar way.

$$\begin{cases} 0 \leq \xi_3 < \rho_m, \text{ specular reflection} \\ \rho_m \leq \xi_3 \leq 1.0, \text{ abandoned} \end{cases} \quad (11)$$

The shading is the part of a mirror shadowed by the other mirrors or the receiver, and the blocking is the part of rays which are reflected by a mirror but hit adjacent mirrors. The blocking is illustrated here to show the procedure for judging whether a ray is blocked or not with the help of the sketch in Fig. 1. Firstly, the location (\mathbf{P}_a) hit by a ray on Mirror a (Ma) and the reflected vector (\mathbf{R}_a) at \mathbf{P}_a are transformed from $X_m Y_m Z_m(a)$ to $X_m Y_m Z_m(b)$ and expressed as \mathbf{P}_{ab} and \mathbf{R}_{ab} in Eqs.(12) and (13). Then the equation of the reflected ray in $X_m Y_m Z_m(b)$ can be obtained using \mathbf{P}_{ab} and \mathbf{R}_{ab} . Finally, the intersection of the ray and Mirror b (Mb) can be calculated by solving the equations of the ray and Mb surface. If the intersection is within Mb , this ray is blocked. The shading process can be computed in the similar way as that given in Ref.[37].

$$\begin{aligned} \mathbf{P}_{ab} = & \begin{bmatrix} 1 & 0 & 0 \\ 0 & \cos \theta_m(b) & \sin \theta_m(b) \\ 0 & -\sin \theta_m(b) & \cos \theta_m(b) \end{bmatrix} \cdot \left\{ \begin{bmatrix} 1 & 0 & 0 \\ 0 & \cos \theta_m(a) & -\sin \theta_m(a) \\ 0 & \sin \theta_m(a) & \cos \theta_m(a) \end{bmatrix} \cdot \mathbf{P}_a \right. \\ & \left. + \begin{bmatrix} 0 \\ y_m(a) - y_m(b) \\ 0 \end{bmatrix} \right\} \end{aligned} \quad (12)$$

$$\mathbf{R}_{ab} = \begin{bmatrix} 1 & 0 & 0 \\ 0 & \cos \theta_m(b) & \sin \theta_m(b) \\ 0 & -\sin \theta_m(b) & \cos \theta_m(b) \end{bmatrix} \cdot \begin{bmatrix} 1 & 0 & 0 \\ 0 & \cos \theta_m(a) & -\sin \theta_m(a) \\ 0 & \sin \theta_m(a) & \cos \theta_m(a) \end{bmatrix} \cdot \mathbf{R}_a \quad (13)$$

where, $y_m(a)$ and $y_m(b)$ are the y -values of the center lines of Ma and Mb in $X_g Y_g Z_g$.

3.1.3 Simulation of the solar ray transfer in the receiver

When a ray hits the glass plate of the MTCR or the glass envelope in the STRSC, the optical process will be decided by Eq.(14) using a random number (ξ_4). If it is refracted, the unit vector in glass will be calculated using Snell's law[54]. When the ray penetrates the glass, the direction of the vector will be calculated again using Snell's law[55]. If it is reflected specularly, the reflected vector will be calculated by Fresnel's Law.

$$\begin{cases} 0 \leq \xi_4 < \tau_g & , \text{ refraction} \\ \tau_g \leq \xi_4 < 1 - \rho_g & , \text{ absorption} \\ 1 - \rho_g \leq \xi_4 \leq 1 & , \text{ specular reflection} \end{cases} \quad (14)$$

When a ray hits the absorber tube, the optical process will be decided by Eq.(15) using a random number (ξ_5). If it is reflected specularly, the reflection will be calculated by Fresnel's Law. If the ray is reflected diffusely, the reflection will be calculated using Lambert's law. The optical process on the cavity wall in MTCR can be calculated in the similar way as that shown in Ref.[42].

$$\begin{cases} 0 \leq \xi_5 < \rho_{t,d} & , \text{ diffuse reflection} \\ \rho_{t,d} \leq \xi_5 < 1 - \alpha_t & , \text{ specular reflection} \\ \rho_{t,d} + \rho_{t,s} \leq \xi_5 \leq 1 & , \text{ absorption} \end{cases} \quad (15)$$

where $\rho_{t,d}$ and $\rho_{t,s}$ are the diffuse reflectance and specular reflectance of the coating, respectively.

3.1.4 Computation of solar flux and optical efficiency

The quadrilateral meshes are generated on all surfaces in MTCR and STRSC to count the rays absorbed on these surfaces, and the sketches of the meshes are illustrated in Fig. 4. In order to reveal the details of the fluxes on the absorber tubes, the mesh system of 60 circumferential elements \times 200 lengthwise elements for each tube in MTCR and the mesh system of 68 circumferential elements \times 200 lengthwise elements on the tube in STRSC are used, respectively. If a ray is absorbed in the way shown in Eq.(14) or Eq.(15), the ray will be counted in the number of the rays absorbed in the local element ($n_{p,e}$) where the ray is absorbed. The local flux in each element (q_l) will be calculated after the tracing of the last ray by Eq.(16). The Local Concentration Ratio (*LCR*) is defined as the ratio of the local solar flux (q_l) and *DNI* as shown in Eq.(17). The instantaneous optical efficiency ($\eta_{i,opt}$) is defined in Eq.(18).

$$q_l = e_p n_{p,e} / S_e \quad (16)$$

$$LCR = q_l / DNI \quad (17)$$

$$\eta_{i,opt} = Q_i / (DNI_i \cdot L_m W_m n_m) \quad (18)$$

where S_e is the area of local element; Q_i and DNI_i are the real-time power absorbed by the tubes and the instantaneous *DNI*, respectively.

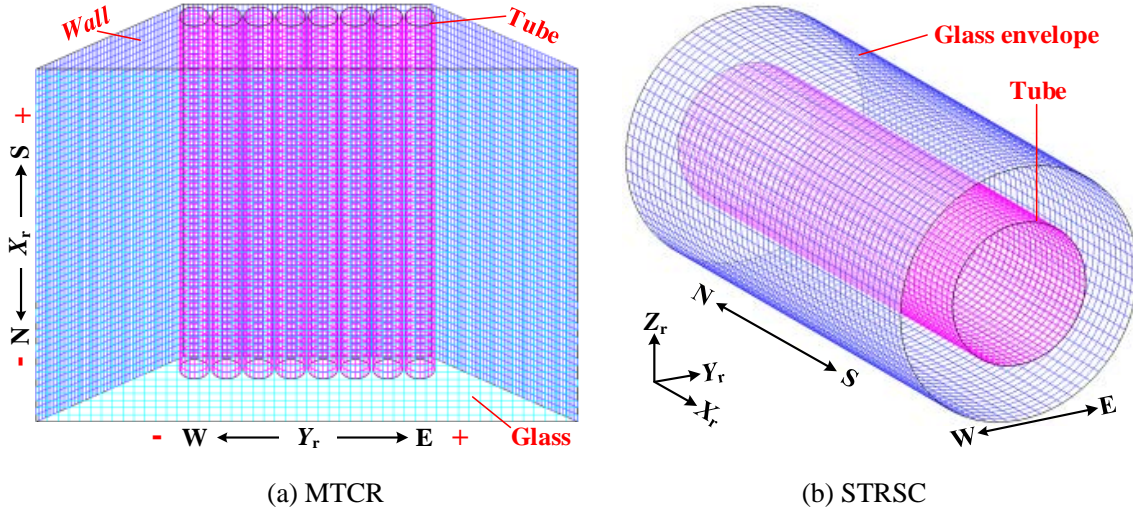


Fig. 4. Sketches of the meshes in MTCR and STRSC.

3.2 Optimization model based on genetic algorithm

Genetic algorithm (GA) first presented by Prof. John Henry Holland in 1975 is a kind of evolutionary algorithm which imitates the processes of biology evolution in nature[56], and it is viewed as an effective method for optimization problems[57-59]. In current model, a real coded GA called MI-LXPM[60] is used to solve current integer constrained problem. The genetic operators including tournament selection, extended Laplace crossover and extended power mutation are applied to produce the new population from the old one, and this process will be repeated for plenty of generations until the best individual is produced. The main procedures of MI-LXPM are summarized as:

- (1) A population with N individuals is randomly initialed, and there are n_m genes in each individual.
- (2) The fitness function (f_{MT} or f_{ST}) for each individual is evaluated.
- (3) Check the stop criterion. If it is satisfied, the optimization will stop. Otherwise, it will go to step 4.
- (4) Selects members from initial or old population using tournament selection operator to make mating pool.
- (5) Extended Laplace crossover is used to produce two new individuals using a pair of parents in the mating pool, followed by the extended power mutation which alters the gene in the new individuals randomly to produce the offspring[54].
- (6) A truncation procedure is applied to ensure the integer restrictions[54]. The new population is regarded as the old one, and the algorithm continues from step 2.

3.2.1 Population initialization

A population with N individuals is randomly initialized, and each individual (g) is stored in a vector of n_m integer numbers (g_i) as expressed in Eq.(19), where each g_i is the ordinal number of the aiming line for corresponding i th mirror. The lower and upper bounds for g_i are g_i^L and g_i^U , respectively. In current optimization, $N=25$.

$$g = (g_1, g_1, \dots, g_{n_m}) \quad (19)$$

3.2.2 Stop criterion and selection

If the relative change in the best fitness function (f_{MT} or f_{ST}) over 50 is less than 1×10^{-6} , the optimization stops. Otherwise, tournament selection operator is used for selecting the best individuals from the old population. In this selection, tournaments are run among three randomly chosen individuals, and the individual with the lowest f_{MT} or f_{ST} is selected. This process will continue until N new individuals are selected, and these individuals will constitute a new population.

3.2.3 Crossover and mutation

A crossover operator called extended Laplace crossover is used to produce the offspring by producing the genes ($g_i^{(1)}, g_i^{(2)}$) of two children from the corresponding genes ($g_i^{(1)}, g_i^{(2)}$) of a pair of parents in the way shown in Eqs. (20) and (21)[60, 61]. The crossover probability (p_c) determinates how often it is performed.

$$\begin{cases} g_i^{(1)} = g_i^{(1)} + \beta_i |g_i^{(1)} - g_i^{(2)}| \\ g_i^{(2)} = g_i^{(2)} + \beta_i |g_i^{(1)} - g_i^{(2)}| \end{cases} \quad (20)$$

$$\beta_i = \begin{cases} a_c - b_c \ln(\xi_i), \varepsilon_i \leq 0.5 \\ a_c + b_c \ln(\xi_i), \varepsilon_i > 0.5 \end{cases} \quad (21)$$

where β_i is a random number which follows the Laplace distribution; ε_i and ξ_i are two independent uniform random numbers within 0 and 1; a_c and b_c are location and scaling parameters, respectively. In current optimization, $p_c=0.8$, $a_c=0$, and $b_c=0.35$.

After the crossover process, a mutation operator called extended Power mutation is performed to mutate the individuals, and the mutation probability (p_m) determinates how often it is performed on the old population[60, 62]. When it is performed, a muted solution g_k'' is created in the vicinity of a parent solution g_k' in the way shown in Eq.(22). In current optimization, $p_m=0.01$.

$$g_k'' = \begin{cases} g_k' - s \cdot (g_k' - g_k^L), t < \varepsilon_k \\ g_k' + s \cdot (g_k^U - g_k'), t \geq \varepsilon_k \end{cases} \quad (22)$$

$$s = (\xi_k)^{p_{mt}}, t = (g_k' - g_k^L) / (g_k^U - g_k^L)$$

where ξ_k is a uniform random number between 0 and 1; g_k^L and g_k^U are the lower and upper

bounds of k th gene; p_{int} is called the index of mutation. In current optimization, $p_{\text{int}}=4$.

3.2.4 Truncation procedure

The truncation procedure is applied to ensure the integer restrictions of the genes, and the gene g'_i after crossover and mutation is truncated to integer value $g'_{i,\text{int}}$ by Eq.(23)[60].

$$g'_{i,\text{int}} = \begin{cases} g'_i, & \text{if } g'_i \text{ is integer} \\ \begin{cases} \lceil g'_i \rceil + 1, & \xi_i \leq 0.5 \\ \lfloor g'_i \rfloor - 1, & \xi_i > 0.5 \end{cases}, & \text{otherwise} \end{cases} \quad (23)$$

where $\lceil g'_i \rceil$ is the integer part of g'_i .

4. Model validation

The MCRT model was validated in the following way. Firstly, the *LCR* profile on the focal plane of a LFR with 30 mirrors was calculated under normal incidence and compared with the experimental result provided by Chemisana, et al.[63] as shown in Fig. 5, where $\sigma_{\text{se}}=12.5$ mrad. It is seen that two curves agree quite well with each other, and the relative deviations are less than 1.6%. Furthermore, the *LCR* profiles on the tubes of the MTCR in current LFR were computed at normal incidence and compared with those computed using SolTrace[64], where strategy S2 is used with $W_{\text{aim}}=240$ mm, and the diffuse reflection in MTCR in current MCRT model is treated as specular reflection, which is the same as that in SolTrace. Fig. 6 illustrates the comparison of the results. It is seen that the *LCR* profiles of the present model agree with those of SolTrace well on both tube 1 and tube 4 in Fig. 2(a), respectively. These good agreements with both experimental and simulation results indicate that the current model is reliable.

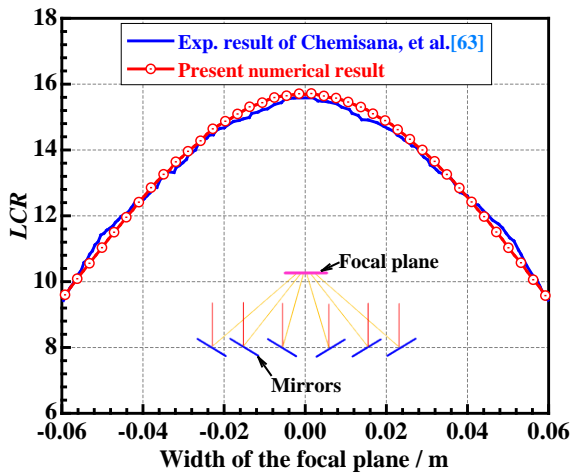


Fig. 5. Comparison of present result and experimental result in Ref.[63].

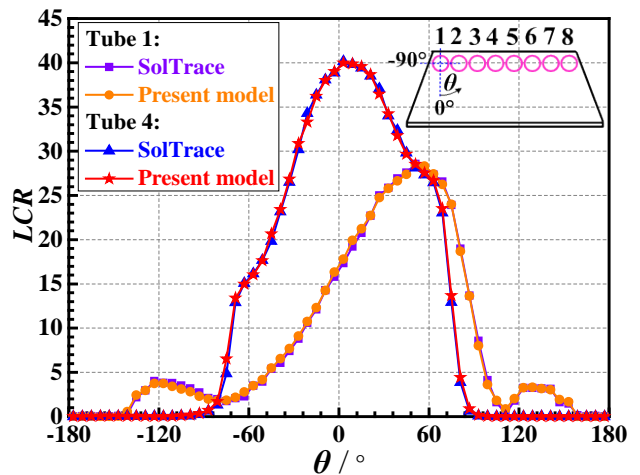


Fig. 6. Comparison of the results between present model and SolTrace.

5. Results and discussion

5.1 Optimization results of solar flux distributions

A typical condition with the solar latitude (α_s) of 45° and solar azimuth (A_s) of 90° is taken as an example to show the typical optimization results of the solar flux distributions, where the solar altitude's projection ($\alpha_{s,p}$) is equal to α_s . Fig. 7 shows the variation of the fitness functions (f_{MT}, f_{ST}) with respect to the number of generations. In the optimizations, $W_{aim}=280$ mm and $n_{aim}=11$ for the LFR with a MTCR, while $W_{aim}=200$ mm and $n_{aim}=11$ for the LFR with a STRSC. It is seen that the fitness functions decrease with the increasing generation number, and the optimizations are terminated after 95 and 123 generations for the two LFRs, respectively. Table 2 shows the optimization results of the aiming strategies for the two LFRs at this typical condition.

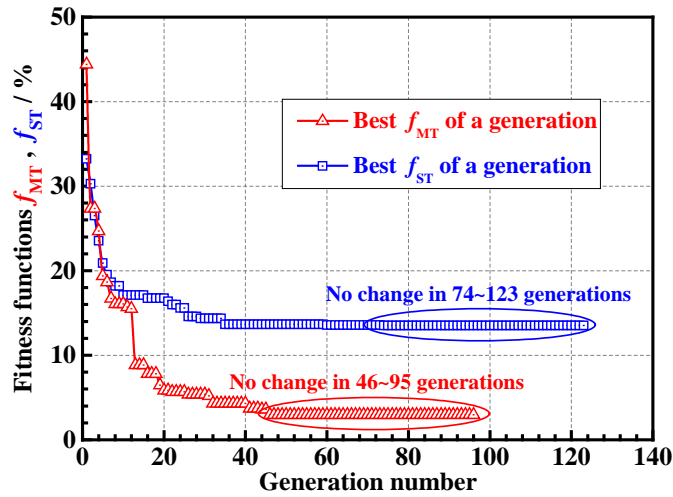


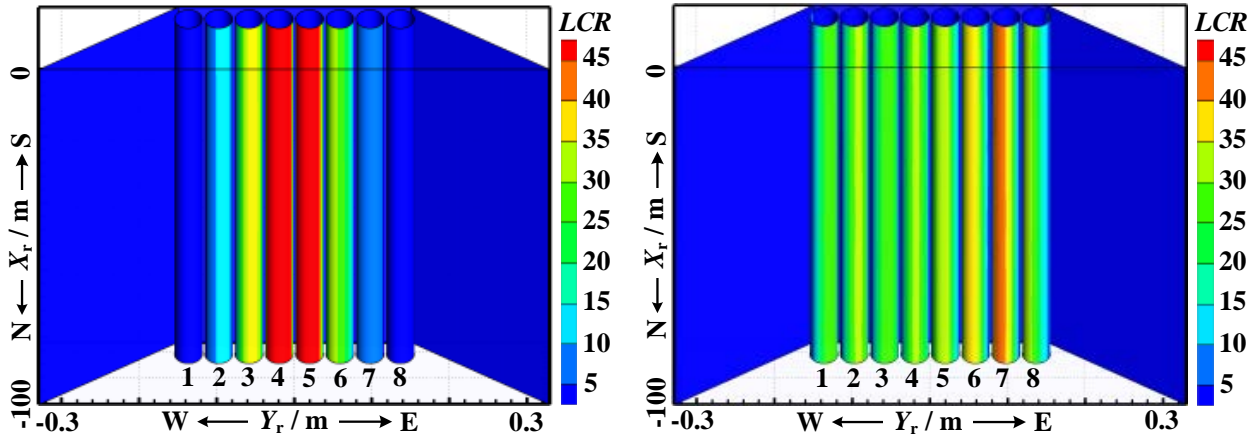
Fig. 7. Variation of the fitness functions (f_{MT}, f_{ST}) with the generation number.

Table 2 Optimization results of the aiming lines for the LFR using a MTCR or STRSC when $\alpha_s=45^\circ$ and $A_s=90^\circ$.

MTCR, $W_{aim}=280$ mm, $n_{aim}=11$	Mi	1	2	3	4	5	6	7	8	9	10	11	12	13
	Ai	1	11	7	10	3	9	9	8	8	8	8	8	7
	Mi	14	15	16	17	18	19	20	21	22	23	24	25	-
	Ai	1	4	2	6	9	3	4	4	8	4	8	7	-
STRSC, $W_{aim}=200$ mm, $n_{aim}=11$	Mi	1	2	3	4	5	6	7	8	9	10	11	12	13
	Ai	1	1	2	4	10	4	10	5	5	8	6	5	7
	Mi	14	15	16	17	18	19	20	21	22	23	24	25	-
	Ai	10	3	8	10	8	2	4	7	8	5	7	5	-

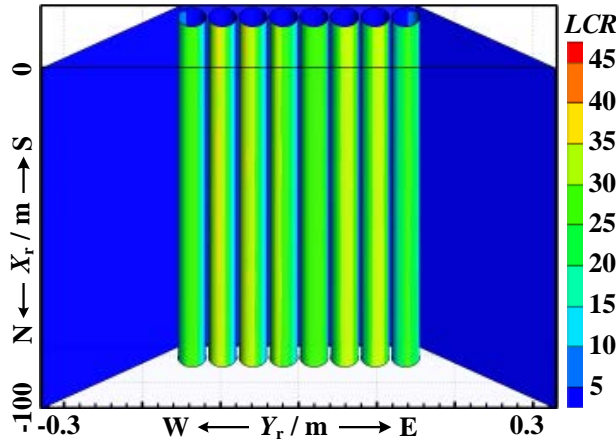
Fig. 8 illustrates the *LFR* distributions in the MTCR for three aiming strategies. It is seen in Fig. 8(a) that the energy maldistribution is significant for S1 with $f_{MT}=100.5\%$, where most rays shine on tubes 4 and 5, while tubes 1 and 8 are barely utilized. As a result, the LCR_{max} of 88.5 appears on tube

5. It is seen in Fig. 8(b) that the energy maldistribution can be refined by S2 with $f_{MT}=14.1\%$. However, a hot region can still be observed on tubes 6 and 7, where LCR_{max} of 44.0 appears on tube 7. It is seen in Fig. 8(c) that the flux for S3 is quite uniform with $f_{MT}=3.1\%$ and LCR_{max} of 36.0 on tube 7, where the drops in f_{MT} are 96.9% and 78.0% compared to those of S1 and S2, respectively. And the corresponding drops in LCR_{max} are 59.3% and 18.2%, respectively. In addition, it is also found that the instantaneous optical efficiency ($\eta_{i,opt}$) for S3 is 1.2 percent lower but 2.0 percent higher than those of S1 and S2, respectively.



(a) S1: $f_{MT}=100.5\%$, $LCR_{max}=88.5$, $\eta_{i,opt}=69.3\%$.

(b) S2 with $W_{aim}=280$ mm:
 $f_{MT}=14.1\%$, $LCR_{max}=44.0$, $\eta_{i,opt}=66.1\%$.



(c) S3 with $W_{aim}=280$ mm, $n_{aim}=11$: $f_{MT}=3.1\%$, $LCR_{max}=36.0$, $\eta_{i,opt}=68.1\%$

Fig. 8. Solar flux distributions in MTCR for three aiming strategies, $\alpha_s=45^\circ$ and $A_s=90^\circ$.

Fig. 9 and Fig. 10 show the LFR distributions on the absorber tube in the STRSC for three aiming strategies. It is seen in Fig. 9(a) that the solar flux is significantly non-uniform for S1 with $f_{ST}=66.3\%$ and $LCR_{max}=96.4$, where only 21.9% of the total power shines on the top half of the tube. It is seen in Fig. 9(b) that the non-uniform flux is refined by S2 with $f_{ST}=38.3\%$. However, a hot region can still be observed at about $\theta=110^\circ$ with $LCR_{max}=67.2$. It is seen in Fig. 8(c) that the flux

for S3 is quite uniform with $f_{ST}=13.5\%$ and $LCR_{max}=51.7$, where f_{ST} is reduced by 79.6% and 64.8% compared to those of S1 and S2, respectively. And the corresponding drops in LCR_{max} are 46.4% and 23.1%, respectively. It is worth noting that 53.1% of the total power is on the top half for S3, which could greatly reduce the bending of the tube and protect the glass envelope from vacuum failure. It is also seen that the drops in $\eta_{i,opt}$ for S2 and S3 are 8.6 percent and 8.8 percent compared to that of S1, respectively. This is because some rays are lost through the gap between the top of the absorber and CPC after being reflected by CPC when S2 and S3 are used. This large gap is inherent due to the use of the glass envelope, so it is hard to reduce this loss when S2 or S3 is used. For improving the optical efficiency, it is suggested that the present GA optimization strategy can be used when the solar radiation is relatively large or the temperature is relatively high, while it is better to use S1 under the opposite conditions.

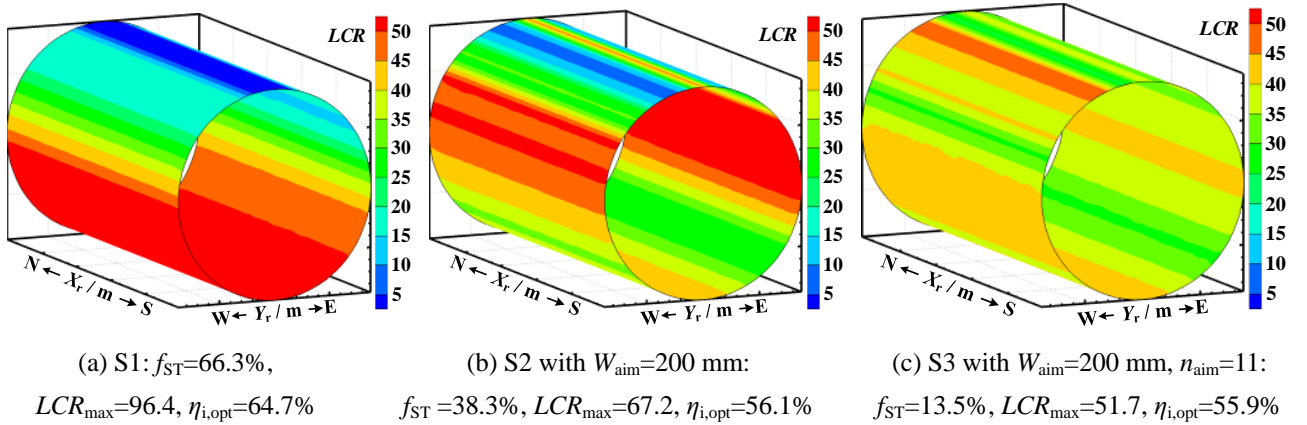


Fig. 9. Solar flux distributions in STRSC for three aiming strategies, $\alpha_s=45^\circ$ and $A_s=90^\circ$.

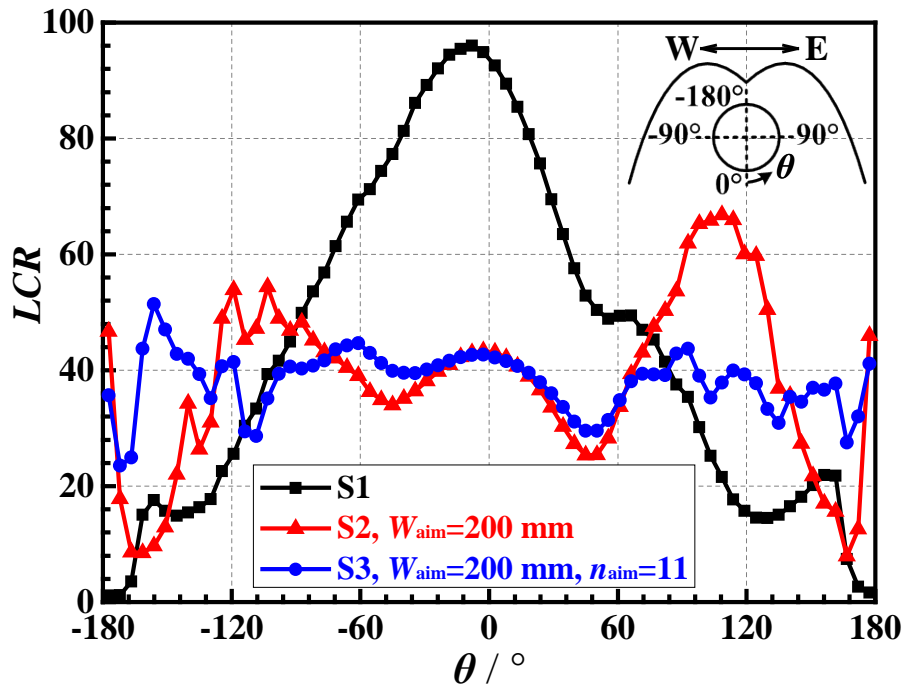


Fig. 10. Comparison of flux profiles in STRSC for three aiming strategies, $\alpha_s=45^\circ$ and $A_s=90^\circ$.

These results indicate that the local high flux in the receivers can be successfully homogenized by the proposed GA optimization approach, which shows a promising way for solving the local high temperature that may accelerate the degradation of coating and the high thermal stress which could lead to the damage of glass envelope. It also seen that the energy maldistribution among tubes in MTCR is almost eliminate, which can weaken negative effects caused by the unstable operation due to the uneven heating of the fluid among the tubes.

5.2 Effect of the width of aiming plane

Fig. 8(c) and Fig. 11 show the optimization results of the solar fluxes in MTCR for different widths of aiming plane when $\alpha_s=45^\circ$ and $A_s=90^\circ$. It is found that a drop in $\eta_{i,opt}$ of 3.2 percent can be observed for $W_{aim}=240$ mm in Fig. 11(a) as compared to that of $W_{aim}=280$ mm in Fig. 8(c), while the variations of f_{MT} and LCR_{max} are not obvious. This is because more mirrors are trying to shining the aiming lines near the two sides for homogenizing the energy maldistribution. As a result, more rays are lost. It is also seen that the energy maldistribution becomes more obvious when $W_{aim}=200$ mm, and tubes 1 and 8 are barely utilized. This is because the width is too short to homogenize the flux. Moreover, the variation of $\eta_{i,opt}$ is not obvious. It is because few rays are lost for this short aiming plane.

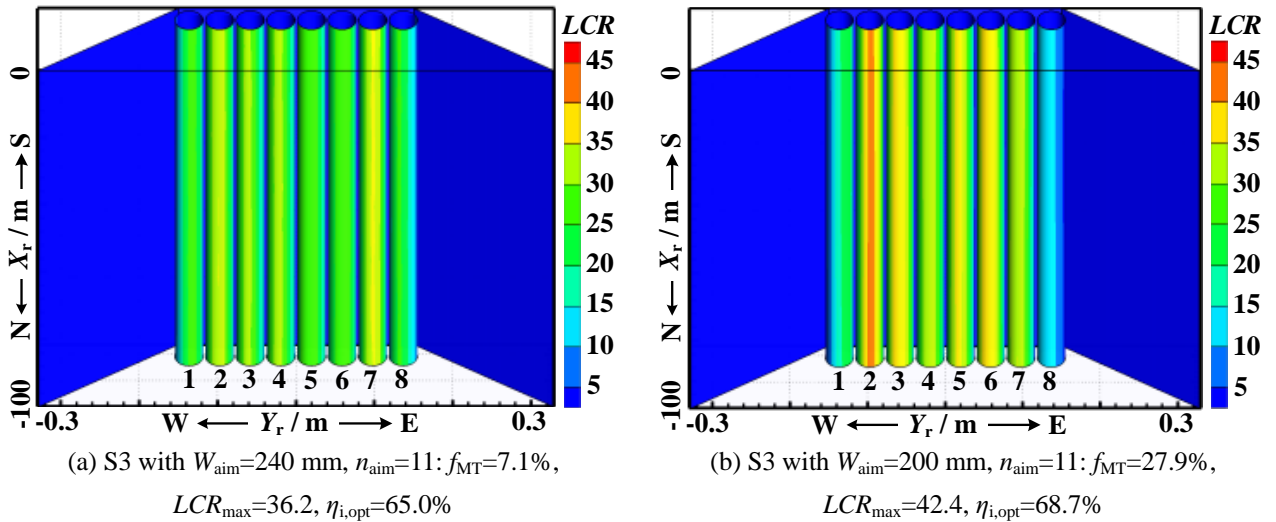


Fig. 11. Effect of the width of aiming plane on solar flux distribution in MTCR, $\alpha_s=45^\circ$ and $A=90^\circ$.

Fig. 12 shows the optimization results of the solar fluxes in STRSC for different widths of aiming plane. It is seen that the distributions vary insignificantly for $W_{aim}=160\sim 240$ mm. This is due to the help of CPC which redistributes the flux. A drop in efficiency is also observed for

$W_{\text{aim}}=240\text{mm}$ as compared to those of other widths. Moreover, the non-uniformity becomes more obvious when $W_{\text{aim}}=120\text{ mm}$, and an increase in efficiency is also observed.

The above results indicate that the width of the aiming plane should be within a suitable range for both MTCR and STRSC. For following discussion, $W_{\text{aim}}=280\text{ mm}$ and $W_{\text{aim}}=200\text{ mm}$ are used for MTCR and STRSC, respectively.

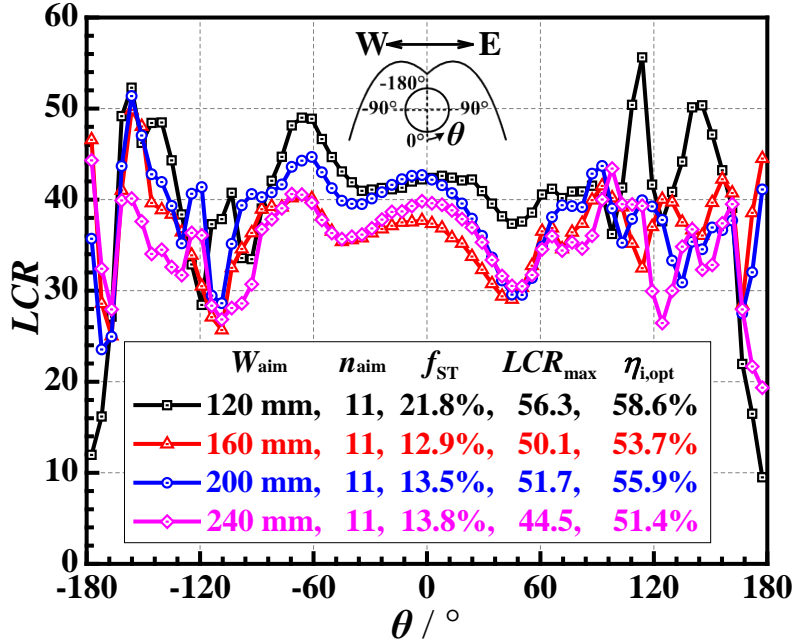
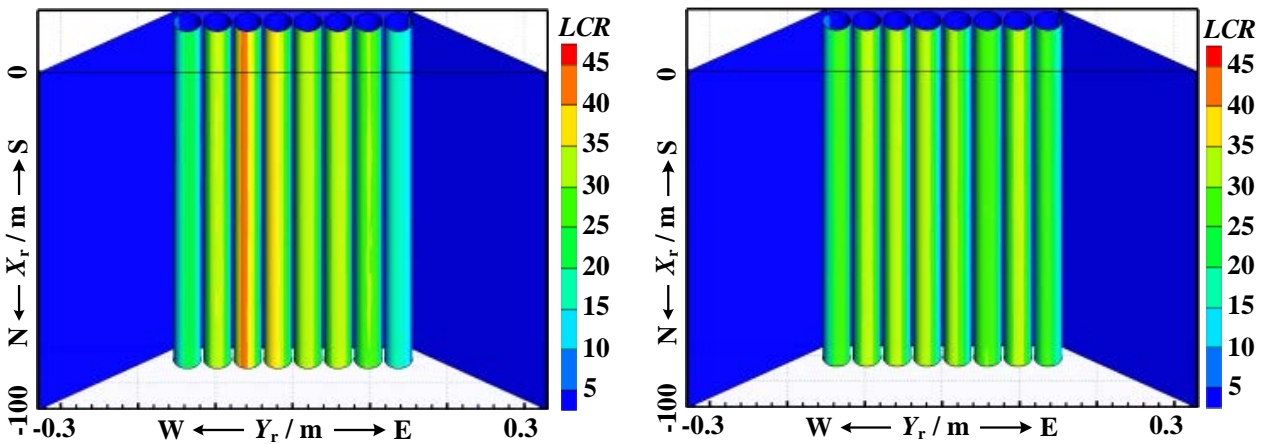


Fig. 12. Effect of the width of aiming plane on solar flux distribution in STRSC, $\alpha_s=45^\circ$ and $A_s=90^\circ$.

5.3 Effect of the number of aiming lines

Fig. 8(c) and Fig. 13 show the solar flux distributions in MTCR for different numbers of aiming lines with $\alpha_s=45^\circ$ and $A_s=90^\circ$. It is seen that flux becomes more non-uniform for $n_{\text{aim}}=7$ in Fig. 13 (a) as compared to that of $n_{\text{aim}}=11$ in Fig. 8(c). It is also seen that the difference between the flux distributions for $n_{\text{aim}}=25$ in Fig. 13(b) and $n_{\text{aim}}=11$ in Fig. 8(c) is not obvious. The comparison also indicates that the number of aiming lines influences little on optical efficiency.



(a) S3 with $W_{\text{aim}}=280$ mm, $n_{\text{aim}}=7$: $f_{\text{MT}}=19.6\%$,
 $LCR_{\text{max}}=42.0$, $\eta_{i,\text{opt}}=68.1\%$

(b) S3 with $W_{\text{aim}}=280$ mm, $n_{\text{aim}}=25$: $f_{\text{MT}}=1.5\%$,
 $LCR_{\text{max}}=34.9$, $\eta_{i,\text{opt}}=67.0\%$

Fig. 13. Effect of the number of aiming lines on solar flux distribution in MTCR, $\alpha_s=45^\circ$ and $A_s=90^\circ$.

Fig. 14 shows the LCR distributions in STRSC for different numbers of aiming lines with $\alpha_s=45^\circ$ and $A_s=90^\circ$. In general, it is seen that the influence of the number of aiming lines on both the flux distribution and the optical efficiency is insignificant when $n_{\text{aim}}=7\sim 25$. However, the effects on uniformity and efficiency become significant when n_{aim} is smaller than 7. From above results, it can be concluded that a suitable number of aiming lines is necessary for obtaining both relatively high efficiency and uniform flux distribution. In following discussion, $n_{\text{aim}}=11$ is used for both MTCR and STRSC.

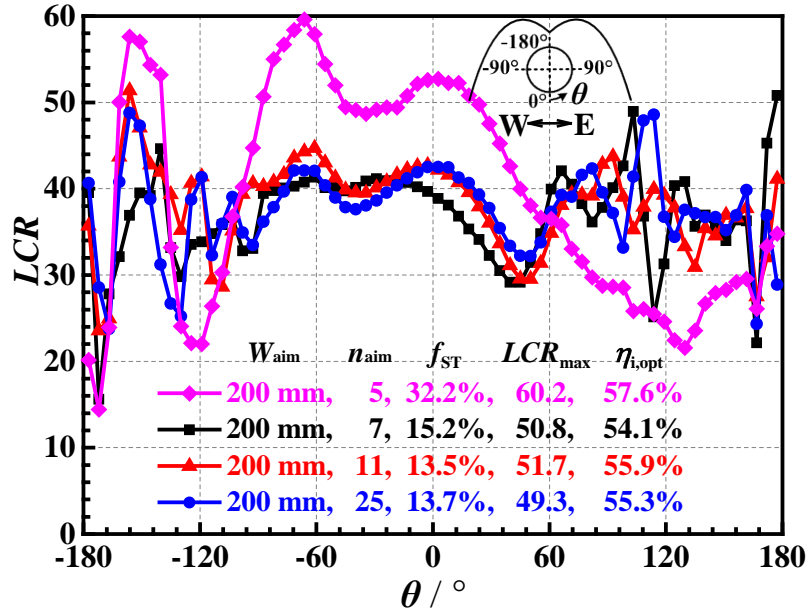


Fig. 14. Effect of the number of aiming lines on solar flux distribution in STRSC, $\alpha_s=45^\circ$ and $A_s=90^\circ$.

5.4 Application of GA optimization strategy under a real-time condition

It is important for an aiming strategy to obtain sufficiently good results at any time rather than just a specific time point. So, the GA optimization strategy (S3) is applied in the two LFRs at different incident angles on a typical day to illustrate this application under a real-time condition. Firstly, A series of optimization results for different values of the solar altitude's projection ($\alpha_{s,p}$) in Fig. 1 are obtained using S3. Then, the result of a specific $\alpha_{s,p}$ can be used in the LFR at the corresponding local solar time(t_s). For present LFRs, several typical cases on spring equinox are given in Table 3. In the optimizations, $W_{\text{aim}}=280$ mm and $n_{\text{aim}}=11$ for the LFR with a MTCR, while

$W_{\text{aim}}=200$ mm and $n_{\text{aim}}=11$ for the LFR with a STRSC.

Table 3 Typical cases for applying the optimization strategy under a real-time condition (spring equinox).

Case	t_s /h	$\alpha_{s,p}/^\circ$	$A_s/^\circ$	$\alpha_s/^\circ$
1	6.716	10.0	94.0	10.0
2	7.434	20.0	98.6	19.8
3	8.138	30.0	103.7	29.3
4	8.822	40.0	109.6	38.3
5	9.158	45.0	113.0	42.6
6	9.488	50.0	116.9	46.8
7	10.136	60.0	126.4	54.4
8	10.766	70.0	139.5	60.7
9	11.386	80.0	157.5	65.2
10	12.000	90.0	180.0	66.9

Fig. 15 shows the real-time optimization results for the LFR with a MTCR at different $\alpha_{s,p}$ in the morning on spring equinox, where the symmetrical results in the afternoon are omitted. It is seen that f_{MT} is smaller than 5.6% for $\alpha_{s,p}=20^\circ\sim 90^\circ$, and $f_{\text{MT}}=12.1\%$ for $\alpha_{s,p}=10^\circ$. This result indicates that the energy can be distributed almost equally among the tubes in the whole range of the incident angle by the GA approach. It is also seen that $\eta_{i,\text{opt}}$ presents an increasing trend for both S1 and S3, and a decrease in $\eta_{i,\text{opt}}$ of 0.6~4.4 percent for S3 can be found as compared to those of S1. Moreover, it is observed that the maximum flux ($q_{1,\text{max}}$) also presents an increasing trend due to the increases in both $\eta_{i,\text{opt}}$ and DNI , and the highest $q_{1,\text{max}}$ of $35946.0 \text{ W}\cdot\text{m}^{-2}$ appears at $t_s=12\text{h}$ ($\alpha_{s,p}=90^\circ$).

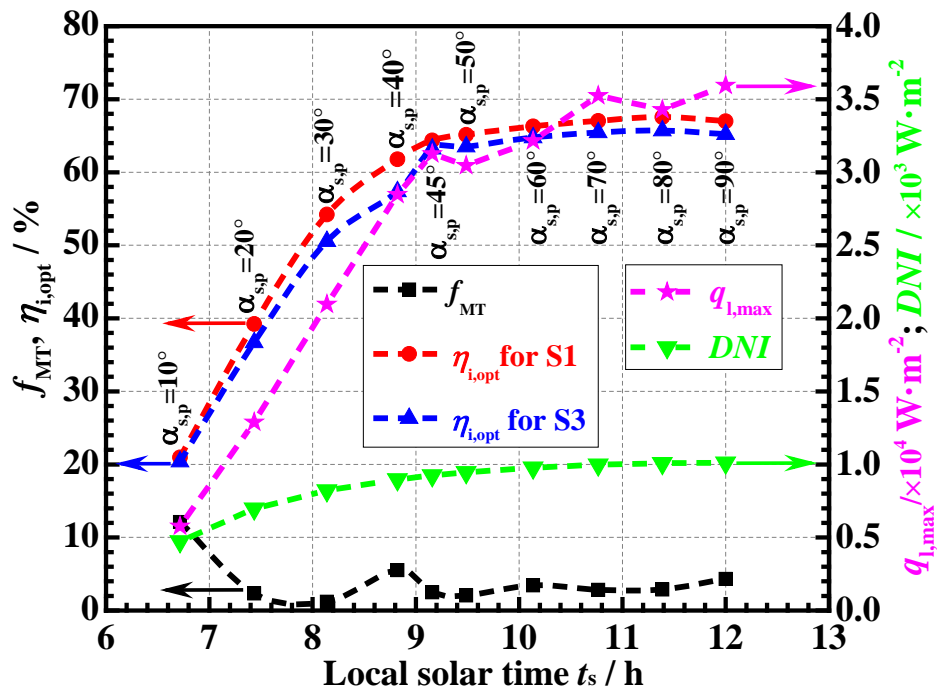


Fig. 15. Real-time optimization results for the LFR with a MTCR on spring equinox.

Fig. 16 shows the typical real-time solar fluxes in the MTCR at $t_s=8.138$ h, 10.136 h and 12 h on spring equinox. It is visually observed that the solar power has been distributed quite well in each case, and no hot spot occurs on the tubes. It can also be found that the southern ends of the tubes are barely shone. Because the rays generally come from the south, and the rays reflected by the southern ends of the mirrors will not hit the southern ends of the MTCR, which leads to this end loss.

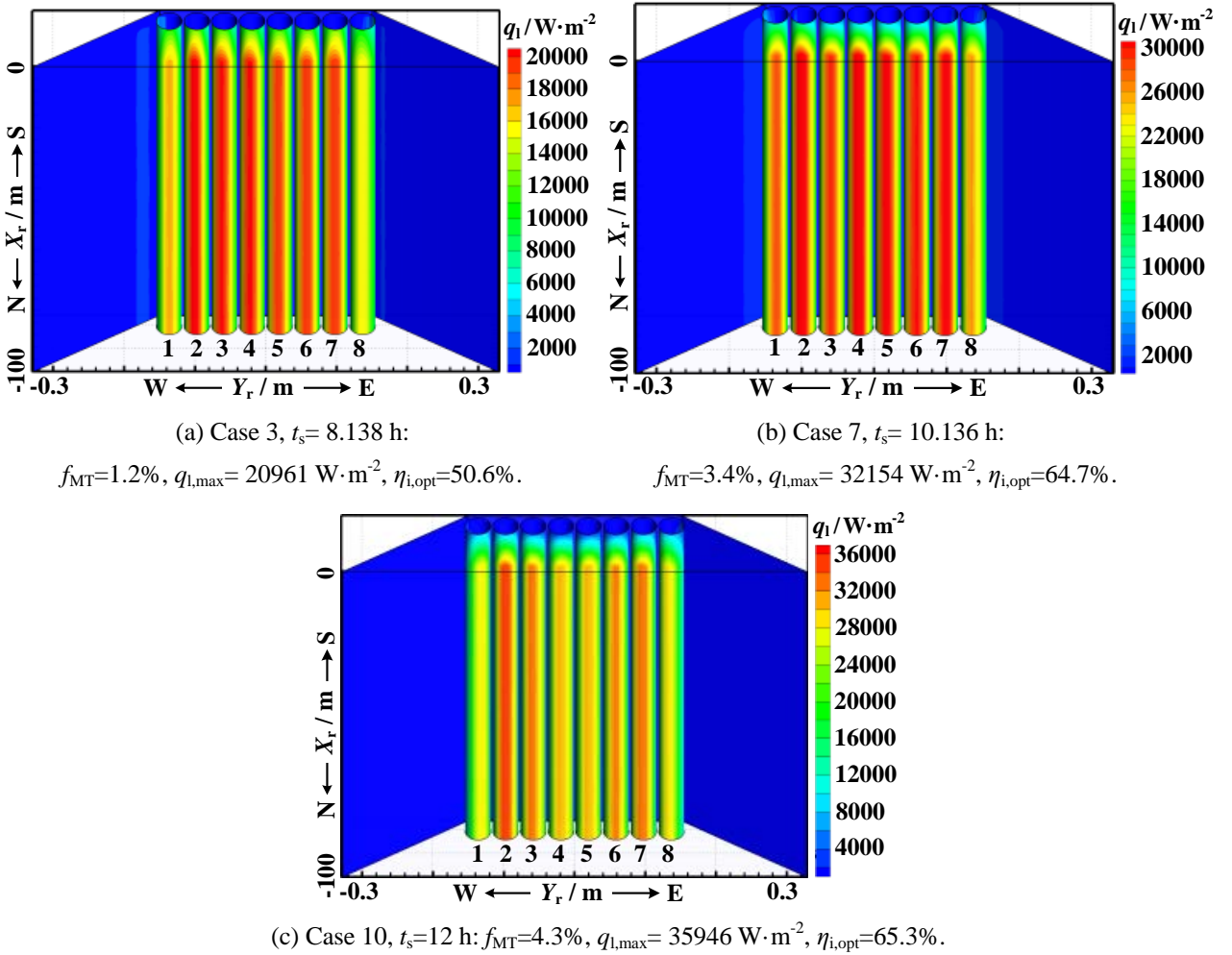


Fig. 16. Real-time solar flux distributions in MTCR on spring equinox.

Fig. 17 shows the real-time optimization results for the LFR with a STRSC on spring equinox. It is seen that f_{ST} is in the range of 11.9%~21.0% for $\alpha_{s,p}=10^\circ\sim 90^\circ$, which indicates that the flux on the absorber tube is quite uniform. It is also seen that $\eta_{i,opt}$ and $q_{1,max}$ present increasing trends with time in the morning. Furthermore, an obvious decrease in $\eta_{i,opt}$ of 0.4~11.0 percent for S3 as compared to that of S1 can be observed, which is due to the inherent large gap between the absorber and the CPC as explained in section 5.1. In addition, it is observed that the highest $q_{1,max}$ of 52600.5

$W \cdot m^{-2}$ appears at $t_s=11.386h$ ($\alpha_{s,p}=80^\circ$).

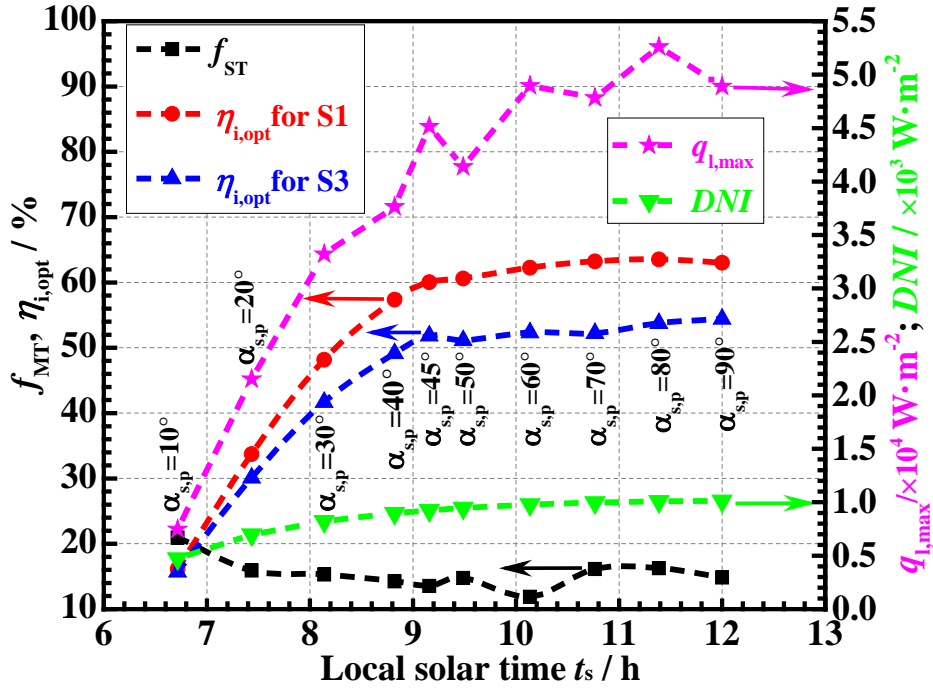
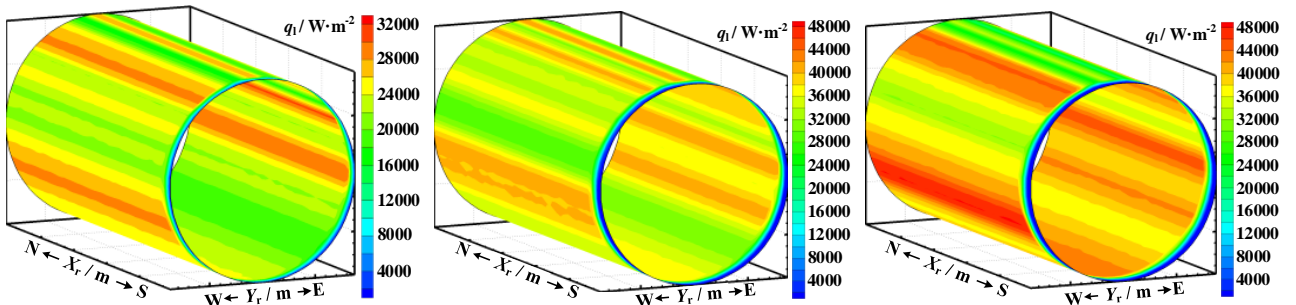


Fig. 17. Real-time optimization results for the LFR with a STRSC on spring equinox.

Fig. 18 and Fig. 19 show the typical real-time solar fluxes in the STRSC at $t_s=8.138 h$, $10.136 h$ and $12 h$ on spring equinox. It is seen in Fig. 18 that the solar flux is quite uniform in each case, and the whole surface of the tube is utilized. Moreover, the end loss at the southern end of the tube can also be observed. It can be further found in Fig. 19 that the solar power is distributed quite well around the tube for each case, and about 46%~48% of the total power is shone on the top half of the tube.



(a) Case 3, $t_s=8.138 h$: $f_{ST}=15.3\%$, $q_{1,max}=33209 W \cdot m^{-2}$, $\eta_{i,opt}=41.7\%$
 (b) Case 7, $t_s=10.136 h$: $f_{ST}=11.9\%$, $q_{1,max}=48957 W \cdot m^{-2}$, $\eta_{i,opt}=52.3\%$
 (c) Case 10, $t_s=12 h$: $f_{ST}=14.8\%$, $q_{1,max}=48897 W \cdot m^{-2}$, $\eta_{i,opt}=54.4\%$

Fig. 18. Real-time solar flux distributions in STRSC on spring equinox.

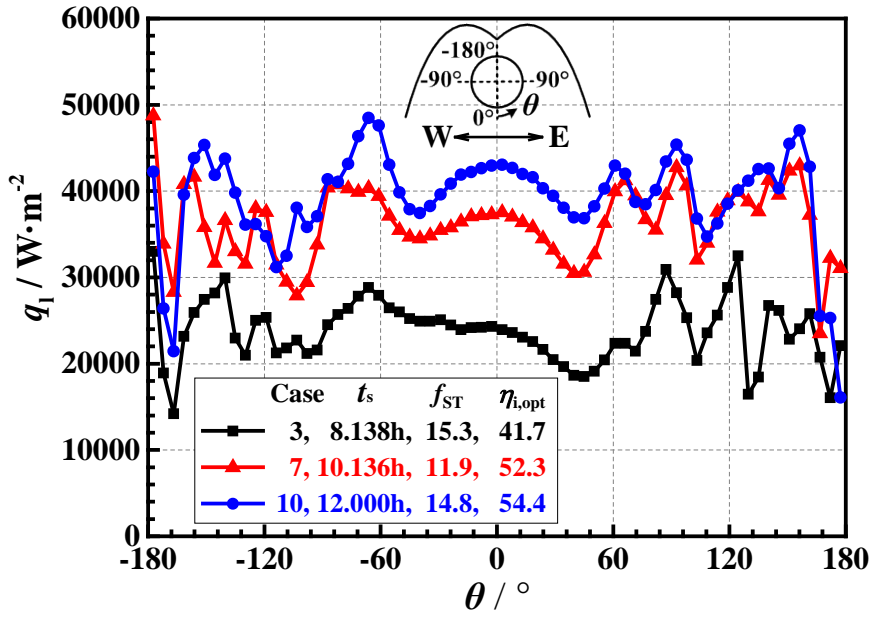


Fig. 19. Details of the flux profiles in STRSC on spring equinox.

6. Conclusions

This work presents an aiming strategy optimization approach for homogenizing the solar flux distributions in both Multi-Tube Cavity Receiver (MTCR) and Single-Tube Receiver with a Secondary Collector (STRSC) in linear Fresnel reflectors. In the approach, the solar fluxes in the receivers are computed using a Monte Carlo ray tracing (MCRT) model, and the optimization is conducted based on Genetic Algorithm (GA). The MCRT model was validated against both experimental and simulation results. The following conclusions are derived.

(1) The GA optimization approach can greatly reduce the energy maldistribution among the tubes in MTCR. The energy maldistribution index (f_{MT}) of 3.1% is achieved at the typical condition. f_{MT} is reduced by 96.9% and 78.0% compared to those of traditional one-line and multi-line strategies (S1, S2), respectively, and the corresponding drops in peak fluxes are 59.3% and 18.2%, respectively, where the variations in efficiency are quite tiny. Moreover, this GA approach can also effectively homogenize the circumferential flux in STRSC, and the non-uniformity index of the flux (f_{ST}) is reduced by 79.6% and 64.8% as compared to those of S1 and S2, respectively, achieving 13.5%. Corresponding drops in peak fluxes are 46.4% and 23.1%, respectively. It is also worth noting that around 50% of the total power can be concentrated on the upper half of the tube by this approach.

(2) The width of the aiming plane and the number of the aiming lines influence both the uniformity of the solar flux in the receivers and the optical efficiency of the LFRs importantly. They

should be designed properly for reaching a compromise between the flux uniformity and optical efficiency.

(3) The application of the GA approach under a real-time condition indicates that satisfactory optimization results can be obtained in the whole range of the incident angle for the sun rays.

(4) These results indicate that the present GA approach is effective and suitable for optimizing the solar flux distributions in the receivers of LFRs.

Acknowledgements

The study is supported by the Key Project of National Natural Science Foundation of China (No.51436007) and the Major Program of the National Natural Science Foundation of China (No. 51590902).

Nomenclature

A_s	solar azimuth ($^{\circ}$)
a_c, b_c	location / scaling parameter in crossover
DNI	Direct Normal Irradiance ($W \cdot m^{-2}$)
d_i	inner diameter of absorber tube (m)
E_t	power absorbed by a tube (W)
e_p	power carried by each ray (W)
f_{ST}	non-uniformity index of circumferential flux (%)
f_{MT}	energy maldistribution index among tubes (%)
g	individual
g_i	gene
H_t	height of absorber tubes (m)
I, N, R	incident / normal / reflection vector
LCR	local concentration ratio
L_m	length of the collector (m)
n_m, n_t	number of mirror / absorber tube
n_{aim}	number of aiming lines
n_g	refraction index of glass
N_p	total number of the traced ray
N	size of population
p_c	crossover probability
p_{int}	index of mutation
Q	power (W)
q	solar flux ($W \cdot m^{-2}$)
R_m	Curvature radius of mirror (m)
S_e	area of each element (m^2)

t_s	solar time (h)
W_{field}	width of the field (m)
W_m	width of the mirror (m)
X, Y, Z	Cartesian coordinates (m)

Greek symbols

α	solar altitude ($^\circ$)
$\alpha_{s,p}$	solar altitude's projection ($^\circ$)
$\alpha_t, \alpha_g, \alpha_w$	absorptivity of coating / glass cover / receiver wall
$\eta_{i,opt}$	instantaneous optical efficiency (%)
θ	angle on the absorber tube ($^\circ$)
θ_m	tracking angle ($^\circ$)
ζ, ε	uniform random number between 0 and 1
ρ_g	specular reflectivity of glass
$\rho_{t,s}, \rho_{t,d}$	specular / diffuse reflectance of coating
$\rho_{w,s}, \rho_{w,d}$	specular / diffuse reflectance of the wall
σ_{se}	slope error of mirror and CPC (mrad)
τ_g	Glass cover transmittance
φ	local latitude ($^\circ$)

Subscripts

d	diffuse parameter
g, l,w,t	glass / local / wall / tube parameter
i	i th parameter
int	integer parameter
s	specular or solar parameter

References

- [1] McGlade C, Ekins P. The geographical distribution of fossil fuels unused when limiting global warming to 2 degrees C. *Nature* 2015; 517: 187-90.
- [2] Li MJ, Song CX, Tao WQ. A hybrid model for explaining the short-term dynamics of energy efficiency of China's thermal power plants. *Appl Energ* 2016; 169: 738-47.
- [3] Li YS. A liquid-electrolyte-free anion-exchange membrane direct formate-peroxide fuel cell. *Int J Hydrogen Energy* 2016; 41: 3600-4.
- [4] Li MJ, Tao WQ. Review of methodologies and polices for evaluation of energy efficiency in high energy-consuming industry. *Appl Energ* 2017; 187: 203-15.
- [5] Li MJ, He YL, Tao WQ. Modeling a hybrid methodology for evaluating and forecasting regional energy efficiency in China. *Appl Energ* 2017; 185: 1769-77.
- [6] Li MJ, Zhao W, Chen X, Tao WQ. Economic analysis of a new class of vanadium redox-flow battery for medium- and large-scale energy storage in commercial applications with renewable energy. *Appl Therm Eng* 2017; doi:10.1016/j.applthermaleng.2016.11.156.
- [7] Qiu Y, He YL, Li P, Du BC. A comprehensive model for analysis of real-time optical performance of a solar power tower with a multi-tube cavity receiver. *Appl Energ* 2017; 185, Part 1: 589-603.

- [8] Kichou S, Abaslioglu E, Silvestre S, Nofuentes G, Torres-Ramírez M, Chouder A. Study of degradation and evaluation of model parameters of micromorph silicon photovoltaic modules under outdoor long term exposure in Jaén, Spain. *Energ Convers Manag* 2016; 120: 109-19.
- [9] Zolfaghari S, Riahy GH, Abedi M, Golshannavaz S. Optimal wind energy penetration in power systems: An approach based on spatial distribution of wind speed. *Energ Convers Manag* 2016; 118: 387-98.
- [10] Wamalwa F, Sichilalu S, Xia X. Optimal control of conventional hydropower plant retrofitted with a cascaded pumpback system powered by an on-site hydrokinetic system. *Energ Convers Manag* 2017; 132: 438-51.
- [11] Michaelides EE. Future directions and cycles for electricity production from geothermal resources. *Energ Convers Manag* 2016; 107: 3-9.
- [12] Mehri S, Shafie-khah M, Siano P, Moallem M, Mokhtari M, Catalão JPS. Contribution of tidal power generation system for damping inter-area oscillation. *Energ Convers Manag* 2017; 132: 136-46.
- [13] Wang J, Yang Y. Energy, exergy and environmental analysis of a hybrid combined cooling heating and power system utilizing biomass and solar energy. *Energ Convers Manag* 2016; 124: 566-77.
- [14] Li YS, Zhao TS. A passive anion-exchange membrane direct ethanol fuel cell stack and its applications. *Int J Hydrogen Energ* 2016; 41: 20336-42.
- [15] Li Y, Lv J, He YL. A Monolithic Carbon Foam-Supported Pd-Based Catalyst towards Ethanol Electro-Oxidation in Alkaline Media. *J Electrochem Soc* 2016; 163: F424-F7.
- [16] Hoffert MI, Caldeira K, Benford G, Criswell DR, Green C, Herzog H, et al. Advanced technology paths to global climate stability energy for a greenhouse planet. *Science* 2002; 298: 981-7.
- [17] Lin M, Sumathy K, Dai YJ, Wang RZ, Chen Y. Experimental and theoretical analysis on a linear Fresnel reflector solar collector prototype with V-shaped cavity receiver. *Appl Therm Eng* 2013; 51: 963-72.
- [18] Wang K, He YL, Cheng ZD. A design method and numerical study for a new type parabolic trough solar collector with uniform solar flux distribution. *SCI CHINA SER E* 2014; 57: 531-40.
- [19] Cheng ZD, He YL, Qiu Y. A detailed nonuniform thermal model of a parabolic trough solar receiver with two halves and two inactive ends. *Renew Energ* 2015; 74: 139-47.
- [20] Zheng ZJ, He Y, He YL, Wang K. Numerical optimization of catalyst configurations in a solar parabolic trough receiver-reactor with non-uniform heat flux. *Sol Energ* 2015; 122: 113-25.
- [21] Wang FQ, Tang ZX, Gong XT, Tan JY, Han HZ, Li BX. Heat transfer performance enhancement and thermal strain restrain of tube receiver for parabolic trough solar collector by using asymmetric outward convex corrugated tube. *Energy* 2016; 114: 275-92.
- [22] Zheng Z, Xu Y, He Y. Thermal analysis of a solar parabolic trough receiver tube with porous insert optimized by coupling genetic algorithm and CFD. *SCI CHINA SER E* 2016; 59: 1475-85.
- [23] Zheng ZJ, He YL, Li YS. An entransy dissipation-based optimization principle for solar power tower plants. *SCI CHINA SER E* 2014; 57: 773-83.
- [24] Zheng ZJ, Li MJ, He YL. Thermal analysis of solar central receiver tube with porous inserts and non-uniform heat flux. *Appl Energ* 2017; 185: 1152-61.
- [25] Cheng ZD, He YL, Cui FQ. Numerical investigations on coupled heat transfer and synthetical performance of a pressurized volumetric receiver with MCRT-FVM method. *Appl Therm Eng* 2013; 50: 1044-54.
- [26] Du BC, He YL, Zheng ZJ, Cheng ZD. Analysis of thermal stress and fatigue fracture for the solar tower molten salt receiver. *Appl Therm Eng* 2016; 99: 741-50.
- [27] Besarati SM, Yogi Goswami D, Stefanakos EK. Optimal heliostat aiming strategy for uniform distribution of heat flux on the receiver of a solar power tower plant. *Energ Convers Manag* 2014; 84: 234-43.
- [28] Hafez AZ, Soliman A, El-Metwally KA, Ismail IM. Solar parabolic dish Stirling engine system design, simulation, and thermal analysis. *Energ Convers Manag* 2016; 126: 60-75.

- [29] Cui FQ, He YL, Cheng ZD, Li YS. Study on combined heat loss of a dish receiver with quartz glass cover. *Appl Energ* 2013; 112: 690-6.
- [30] Tao YB, He YL, Cui FQ, Lin CH. Numerical study on coupling phase change heat transfer performance of solar dish collector. *Sol Energ* 2013; 90: 84-93.
- [31] He YL, Wang K, Du BC, Qiu Y, Liang Q. Non-uniform characteristics of solar flux distribution in the concentrating solar power systems and its corresponding solutions: A review. *Chin Sci Bull* 2016; 61: 3208-37.
- [32] Weinstein LA, Loomis J, Bhatia B, Bierman DM, Wang EN, Chen G. Concentrating Solar Power. *Chem Rev* 2015; 115: 12797-838.
- [33] Wang K, He YL, Qiu Y, Zhang YW. A novel integrated simulation approach couples MCRT and Gebhart methods to simulate solar radiation transfer in a solar power tower system with a cavity receiver. *Renew Energ* 2016; 89: 93-107.
- [34] Zhu Y, Shi J, Li Y, Wang L, Huang Q, Xu G. Design and experimental investigation of a stretched parabolic linear Fresnel reflector collecting system. *Energ Convers Manag* 2016; 126: 89-98.
- [35] Sahoo SS, Singh S, Banerjee R. Steady state hydrothermal analysis of the absorber tubes used in Linear Fresnel Reflector solar thermal system. *Sol Energ* 2013; 87: 84-95.
- [36] Häberle A, Zahler C, de Lalaing J, Ven J, Sureda M, Graf W, et al. The Solarmundo Project. Advanced technology for solar thermal power generation. In: *Solar World Congress, Adelaide, Australia*; 2001.
- [37] Qiu Y, He YL, Cheng ZD, Wang K. Study on optical and thermal performance of a linear Fresnel solar reflector using molten salt as HTF with MCRT and FVM methods. *Appl Energ* 2015; 146: 162-73.
- [38] Balaji S, Reddy KS, Sundararajan T. Optical modelling and performance analysis of a solar LFR receiver system with parabolic and involute secondary reflectors. *Appl Energ* 2016; 179: 1138-51.
- [39] Craig KJ, Moghimi MA, Rungasamy AE, Marsberg J, Meyer JP. Finite-volume ray tracing using Computational Fluid Dynamics in linear focus CSP applications. *Appl Energ* 2016; 183: 241-56.
- [40] Grena R, Tarquini P. Solar linear Fresnel collector using molten nitrates as heat transfer fluid. *Energy* 2011; 36: 1048-56.
- [41] Mills DR, Morrison GL. Compact linear Fresnel reflector solar thermal powerplants. *Sol Energ* 2000; 68: 263-83.
- [42] Qiu Y, He YL, Wu M, Zheng ZJ. A comprehensive model for optical and thermal characterization of a linear Fresnel solar reflector with a trapezoidal cavity receiver. *Renew Energ* 2016; 97: 129-44.
- [43] Moghimi MA, Craig KJ, Meyer JP. A novel computational approach to combine the optical and thermal modelling of Linear Fresnel Collectors using the finite volume method. *Sol Energ* 2015; 116: 407-27.
- [44] Abbas R, Montes MJ, Piera M, Martínez-Val JM. Solar radiation concentration features in Linear Fresnel Reflector arrays. *Energ Convers Manag* 2012; 54: 133-44.
- [45] Abbas R, Montes MJ, Rovira A, Martínez-Val J. Parabolic trough collector or linear Fresnel collector? A comparison of optical features including thermal quality based on commercial solutions. *Sol Energ* 2016; 124: 198-215.
- [46] Montes MJ, Rubbia C, Abbas R, Martínez-Val JM. A comparative analysis of configurations of linear Fresnel collectors for concentrating solar power. *Energy* 2014; 73: 192-203.
- [47] Bellos E, Mathioulakis E, Tzivanidis C, Belessiotis V, Antonopoulos KA. Experimental and numerical investigation of a linear Fresnel solar collector with flat plate receiver. *Energ Convers Manag* 2016; 130: 44-59.
- [48] Qiu Y, He YL, Liang Q, Cheng ZD. A MCRT-FVM simulation method for the coupled photo-thermal conversion process in a Linear Fresnel reflector solar collector. *Journal of Engineering Thermophysics* 2016; 37: 2142-9.
- [49] Dey CJ. Heat transfer aspects of an elevated linear absorber. *Sol Energ* 2004; 76: 243-9.
- [50] Eck M, Uhlig R, Mertins M, Häberle A, Lerchenmüller H. Thermal Load of Direct Steam-Generating Absorber Tubes with Large Diameter in Horizontal Linear Fresnel Collectors. *Heat Transfer Eng* 2007; 28: 42-8.

- [51] Abbas R, Muñoz-Antón J, Valdés M, Martínez-Val JM. High concentration linear Fresnel reflectors. *Energy Convers Manag* 2013; 72: 60-8.
- [52] Serrano-Aguilera JJ, Valenzuela L, Parras L. Thermal 3D model for direct solar steam generation under superheated conditions. *Appl Energy* 2014; 132: 370-82.
- [53] Xu Y, Cui K, Liu D. The development of a software for solar radiation and its verification by the measurement results on the spot. *Energy Tech* 2002; 26: 237-9.
- [54] He YL, Cui FQ, Cheng ZD, Li ZY, Tao WQ. Numerical simulation of solar radiation transmission process for the solar tower power plant: From the heliostat field to the pressurized volumetric receiver. *Appl Therm Eng* 2013; 61: 583-95.
- [55] Qiu Y, Li MJ, He YL, Tao WQ. Thermal performance analysis of a parabolic trough solar collector using supercritical CO₂ as heat transfer fluid under non-uniform solar flux. *Appl Therm Eng* 2016; : DOI:10.1016/j.applthermaleng.2016.09.044.
- [56] Holland JH. *Adaptation in natural and artificial systems: an introductory analysis with applications to biology, control, and artificial intelligence*. Michigan: The University of Michigan Press; 1975.
- [57] Xi H, Li M-J, He Y-L, Zhang Y-W. Economical evaluation and optimization of organic Rankine cycle with mixture working fluids using R245fa as flame retardant. *Appl Therm Eng* 2017; 113: 1056-70.
- [58] Xi H, Li MJ, Xu C, He YL. Parametric optimization of regenerative organic Rankine cycle (ORC) for low grade waste heat recovery using genetic algorithm. *Energy* 2013; 58: 473-82.
- [59] Xi H, Li M-J, He Y-L, Tao W-Q. A graphical criterion for working fluid selection and thermodynamic system comparison in waste heat recovery. *Appl Therm Eng* 2015; 89: 772-82.
- [60] Deep K, Singh KP, Kansal ML, Mohan C. A real coded genetic algorithm for solving integer and mixed integer optimization problems. *Appl Math Comput* 2009; 212: 505-18.
- [61] Deep K, Thakur M. A new crossover operator for real coded genetic algorithms. *Appl Math Comput* 2007; 188: 895-911.
- [62] Deep K, Thakur M. A new mutation operator for real coded genetic algorithms. *Appl Math Comput* 2007; 193: 211-30.
- [63] Chemisana D, Barrau J, Rosell JI, Abdel-Mesih B, Souliotis M, Badia F. Optical performance of solar reflective concentrators: A simple method for optical assessment. *Renew Energy* 2013; 57: 120-9.
- [64] Wendelin T. SolTrace: a new optical modeling tool for concentrating solar optics. In: *ASME 2003 Int Sol Energy Conf.*, Kohala Coast, Hawaii; 2003.